Composite Structures 194 (2018) 252–262

Contents lists available at ScienceDirect

Composite Structures

journal homepage: www.elsevier.com/locate/compstruct

Behavior of steel fiber-reinforced concrete-filled FRP tube columns: Experimental results and a finite element model

Aliakbar Gholampour, Togay Ozbakkaloglu*

School of Civil, Environmental and Mining Engineering, University of Adelaide, SA 5005 Australia

ARTICLE INFO

Keywords:
Steel fiber-reinforced concrete (SFRC)
Fiber-reinforced polymer (FRP)
Confined concrete
Stress-strain relationship
Concentric compression
Finite element (FE) modeling

ABSTRACT

This paper presents the results of an experimental study together with the first finite element (FE) model for the compressive behavior of fiber-reinforced polymer (FRP)-confined steel fiber-reinforced concrete (SFRC). 73 existing experimental test results of FRP-confined and actively confined SFRC specimens tested under axial compression were initially assembled. Additional axial compression tests were conducted on 16 actively confined SFRC specimens to address the gaps in the existing test database to compile a reliable database for the FE modeling of FRP-confined SFRCs. The analysis of experimental test results revealed that the compressive behavior of FRP-confined SFRCs is influenced by the steel fiber volume fraction and aspect ratio. New expressions were developed for the hoop rupture strain of the FRP jacket, axial strain-lateral strain relationship of FRP-confined and actively confined SFRC, and relationship between the confining pressure and the compressive strength of actively confined SFRC by considering the influences of the volume fraction and aspect ratio of internal steel fibers. A recently developed concrete damage-plasticity model, which was shown to be the most accurate currently available model for confined plain concrete, was adopted for the prediction of the compressive behavior of FRP-confined SFRC. The failure surface and flow rule of the model were modified based on the results from actively and FRP-confined SFRC. The results show that model predictions of the axial stress-axial strain, lateral strain-axial strain, axial stress-volumetric strain, plastic volumetric strain-axial plastic strain, and plastic dilation angle-axial plastic strain relationships are in good agreement with the experimental results of FRP-confined SFRC. The new model provides improved accuracy over the best performing existing models of FRP-confined plain concrete in predicting the behavior of FRP-confined SFRC.

1. Introduction

The addition of internal steel fibers to concrete is a popular technique that is used for improving the inherent brittle behavior of plain concrete [1–4]. Likewise, lateral confinement of concrete results in a significant improvement in the ductility of concrete under compression [5–17]. Therefore, fiber-reinforced polymer (FRP)-confined steel fiber-reinforced concrete (SFRC), as an ultra high-performance system, can be considered as a higher performance alternative with further enhanced mechanical properties to conventional FRP-confined plain concrete. As shown previously, the existence of steel fiber decreases isolated major crack formations in the concrete and results in a more even and controlled cracking [18]. In the case of FRP-confined SFRC, this in turn leads to reduced stress concentrations on the FRP jacket leading to higher FRP hoop rupture strains and ductility [19].

A number of experimental studies have been performed recently to understand the mechanical behavior of FRP-confined SFRCs [19–22]. Only the two of these studies experimentally investigated the mechanical behavior of FRP-confined SFRCs under concentric axial compression [19,20]. The remaining two were concerned with FRP-confined SFRC containing internal steel reinforcing bars under eccentric loading [21] and SFRCs confined by hybrid FRP tubes [22]. Existing studies have shown that steel fiber parameters (i.e. volume fraction (V_f) and aspect ratio (A_R)) influence the stress-strain relationship of the concrete. It was shown that at a given V_f, an increase in A_R leads to a decrease in the compressive strength (f'_{cc}), ultimate axial strain (ε_{cu}), and hoop rupture strain ($\varepsilon_{h,rup}$) of concrete. On the other hand, an increase in V_f at a given A_R results in an increase in f'_{cc}, ε_{cu}, and $\varepsilon_{h,rup}$ [19].

Finite element (FE) method has been extensively used to accurately model the mechanical behavior of confined plain concrete. Although a relatively large number of studies have been reported on the FE modeling of FRP-confined plain concrete [23–31], no study has been reported to date on the FE modeling of the FRP-confined SFRC. Furthermore, most of the existing FE models for FRP-confined plain concrete were based on an approach that was recently shown to be inaccurate, especially for high-strength concrete (HSC) [32,33].

* Corresponding author.
E-mail address: togay.ozbakkaloglu@adelaide.edu.au (T. Ozbakkaloglu).

https://doi.org/10.1016/j.compstruct.2018.03.094
Received 3 January 2018; Received in revised form 26 February 2018; Accepted 28 March 2018
Available online 29 March 2018

Therefore, there is a clear need for additional numerical studies to better understand the constitutive behavior of FRP-confined SFRC. As discussed in detail in Refs. [31,34], concrete damage-plasticity approach, which was proposed by Lubliner et al. [35] and later modified by Lee and Fenves [36], provides a more accurate prediction of the constitutive behavior of confined concretes than the pure plasticity and damage approaches. In order to investigate the constitutive behavior of the FRP-confined concrete by damage-plasticity approach, it is required to establish experimental databases for both FRP-confined and actively confined concrete [31]. The review of the literature indicates that only two experimental studies have investigated the compressive behavior of actively confined SFRCs [1,37], the results of which would not be sufficient for the development of an accurate FE model. To address this research gap, in the current study additional experimental tests were performed on actively confined SFRCs to compile a reliable database that would enable FE modeling of FRP-confined SFRCs.

This paper presents the first study on FE modeling of FRP-confined SFRC. Existing experimental test results of FRP-confined and actively confined SFRC specimens tested under axial compression were initially assembled and additional axial compression tests were conducted on actively confined SFRC specimens to address the gaps in the existing test database to provide a reliable database for the constitutive behavior of FRP-confined SFRCs. The new concrete damage-plasticity model with developed failure surface and flow rule is implemented in a FE program ABAQUS [38] through the use of a script (given in Appendix A) for the prediction of: i) axial stress-axial strain, ii) lateral strain-axial strain, iii) axial stress-volumetric strain, iv) plastic volumetric strain-axial plastic strain, and v) plastic dilation angle-axial plastic strain relationships. The FE modeling results show that model predictions are in good agreement with the experimental results of FRP-confined SFRC. Comparisons between the FE modeling and experimental results show that the new model provides improved accuracy compared to the predictions of Lim and Ozbakkaloglu's model [39], which was originally proposed for conventional concrete and shown to provide the most accurate predictions of FRP-confined plain concrete among existing models. The availability of such an accurate model is of vital importance for practical applications of this highly promising FRP-confined SFRC composite system.

2. Experimental test databases

2.1. Existing test database

The databases of FRP-confined and actively confined SFRCs were assembled based on the results available in the open literature. Tables 1 and 2 show the details of these databases. The FRP-confined and actively confined SFRCs databases contained 32 and 41 datasets respectively, obtained from four experimental studies published between 2006 and 2015 [1,19,20,37].

The FRP-confined SFRC database is composed of specimens confined by three types of FRP materials: carbon FRP (CFRP), glass FRP (GFRP), and aramid FRP (AFRP). FRP confinement was provided by manual wet lay-up technique in the hoop direction. The FRP-confined SFRC database presented in Table 1 consists of the following information for each specimen: specimen's geometric properties (diameter D and height H), total fiber thickness (t_f), tensile strength of fibers in FRP jacket (f_f), unconfined concrete strength (f'_{co}), steel fiber volume fraction (V_f), steel fiber aspect ratio ($A_R = l_f/d_f$, where l_f is the steel fiber length and d_f is the equivalent fiber diameter), tensile strength of internal steel fibers (f_{sf}), compressive strength (f'_{cc}), and ultimate axial strain (ε_{cu}). The actively confined SFRC database presented in Table 2 consists of the following information for each specimen: specimen's geometric properties (D and H), f'_{co}, V_f, A_R, f_{sf}, and peak compressive strength (f^*_{cc}) and corresponding axial strain (ε^*_{cc}). Five V_f of 0%, 1%, 1.5%, 2%, and 2.5% and three A_R of 37, 60, and 67 were used in the specimens included in this database.

Table 1
Existing test results of FRP-confined SFRC.

Study	Group	Specimen ID	Specimen Dimension (mm)	FRP Type	t_f (mm)	f_f (MPa)	f'_{co} (MPa)	V_f (%)	A_R	l_f (mm)	d_f (mm)	Steel Fiber Type	f_{sf} (MPa)	f'_{cc} (MPa)	ε_{cu} (%)	$\varepsilon_{h,rup}$ (%)
Xie and Ozbakkaloglu [19]	U120-1	V1.5A67F28	ø152 × 305	AFRP	1.2	2600	131.6	1.5	67	60	0.90	Hooked end	1050	179.8	1.91	1.23
		V1.5A67F27					124.6							171.3	1.78	1.19
		V1.5A67F26					132.7							169.7	1.68	1.14
		V2.5A67F31					123.9	2.5						191.6	2.00	1.37
		V2.5A67F38					131.4							204.7	2.50	1.68
		V2.5A67F26					124.2							191.2	1.95	1.11
	U120-2	V1.5A37F32					124.0	1.5	37	31	0.85	Hooked end	1200	191.8	2.05	1.40
		V1.5A37F33					127.1							188.1	1.82	1.42
		V1.5A37F28					126.4							185.2	1.95	1.20
		V2.5A37F40					122.5	2.5						199.9	2.65	1.75
		V2.5A37F34					126.4							195.3	2.16	1.49
		V2.5A37F42					124.8							204.1	2.31	1.86
	U120-3	V0A0F22					123.5	0	0	–	–	–	–	174.0	2.07	0.96
		V0A0F24					125.7							180.6	2.16	1.07
Zohrevand and Mirmiran [20]	U190-1	V2.0A65F20	ø108 × 191	GFRP	3.06*	610*	194.0	2.0	67	13	0.19	Straight	2800	226.6	0.86	1.20
		V2.0A65F26			4.08*		185.0							273.5	1.06	1.35
		V2.0A65F33			5.10*		190.0							298.9	1.15	1.40
	U190-2	V2.0A65F21		CFRP	2.04*	850*	185.4							254.1	0.68	0.69
		V2.0A65F41			4.08*		185.4							372.2	1.05	0.80

f_f is the tensile strength of fibers in FRP jacket; f_{sf} is the tensile strength of internal steel fibers.
* Properties of FRP tube.

Table 2
Existing test results of actively confined SFRC.

Study	Specimen ID	Specimen Dimension (mm)	f'_{co} (MPa)	V_f (%)	A_R	l_f (mm)	d_f (mm)	Steel Fiber Type	f_{Sf} (MPa)	f^*_{cc} (MPa)	ε^*_{cc} (%)
Lu and Hsu [1]	V0A0F*3.5	ø100 × 200	67.0	0	–	–	–	–	–	84.9	0.47
	V0A0F*7									99.0	0.78
	V0A0F*14									130.7	1.24
	V0A0F*14									132.7	1.25
	V0A0F*14									134.9	1.34
	V0A0F*14									135.5	1.37
	V0A0F*21									154.0	1.66
	V0A0F*21									157.1	1.83
	V0A0F*21									161.2	1.94
	V0A0F*28									180.2	2.50
	V0A0F*28									179.9	2.41
	V0A0F*42									229.1	3.20
	V0A0F*56									276.0	4.10
	V1A60F*7	ø100 × 200	69.0	1	60	30	0.50	Hooked end	1100	105.2	0.71
	V1A60F*14									136.8	1.27
	V1A60F*14									139.0	1.21
	V1A60F*21									164.1	1.70
	V1A60F*21									162.3	2.02
	V1A60F*28									186.5	2.57
	V1A60F*28									189.6	2.74
	V1A60F*28									191.6	2.44
	V1A60F*28									191.8	2.40
	V1A60F*28									189.6	2.52
	V1A60F*42									239.0	3.33
	V1A60F*56									282.2	4.22
	V1A60F*63									308.2	4.51
	V1A60F*70									324.1	4.82

"–" indicates unavailable values in mixes containing no steel fibers.

2.2. New tests on actively confined SFRC specimens

To extend the existing database of actively confined SFRC, four different batches of SFRCs were prepared and confined under hydraulic pressure applied by a Hoek cell. The geometry of the cylindrical specimens was prescribed by the geometry of the Hoek cell (i.e. 63 × 126 mm). Ultra high-strength micro steel fibers with A_R of 73 (l_f = 13 mm and d_f = 0.18 mm) were added to the SFRC mixes at two different V_f of 1% and 2%. Table 3 shows the concrete mix proportions of SFRC specimens. Natural sand and crushed basalt stone with a nominal maximum size of 10 mm were used in the mixes as fine and coarse aggregates, respectively. C50 and C100 mixes were designed to develop a 28-day compressive strength of 50 MPa and 100 MPa and they had a water-to-binder ratio (w/b) of 0.479 and 0.295, respectively. Silica fume was used in C100 mixes to achieve a high compressive strength and polycarboxylic ether polymer-based superplasticizer was used in both C50 and C100 mixes in order to achieve sufficient workability. The workability of fresh SFRC was evaluated by a slump test, which was performed in accordance with ASTM C143/C143M [40].

Constant confining pressures (f'_l) of 5, 10, 15, and 25 MPa were applied on the specimens using a Hoek cell to investigate the effect of different confinement levels ranging from low to high level on the behavior of SFRC. Axial compression tests were conducted with a displacement control at a rate of 0.18 mm/min using a 1000-kN capacity universal testing machine in accordance with ASTM C39/C39M-16b [41]. Fig. 1 shows the instrumentation and test setup of specimens

Table 3
Mix proportions of the concrete.

Concrete Mix	C50-1	C50-2	C100-1	C100-2
Cement (kg/m^3)	375	375	506	506
Silica Fume (kg/m^3)	–	–	44	44
Sand (kg/m^3)	720	720	700	700
Coarse Aggregate (kg/m^3)	1053	1026	1023	996
Water (kg/m^3)	176	176	145	145
Superplasticizer (kg/m^3)	5	5	25	25
w/b *	0.479	0.479	0.295	0.295
Volume Fraction (V_f) (%)	1	2	1	2
Fiber (kg/m^3)	78	156	78	156
Slump (mm)	140	125	175	130

* Including the water coming from the superplasticizer (i.e. 70% water by weight).

Fig. 1. Instrumentation and test setup used in compression tests.

Table 4
28-day compression test results of actively confined SFRC.

Specimens	f'_{co} (MPa)	V_f (%)	A_R	l_f (mm)	d_f (mm)	Steel Fiber Type	f_{Sf} (MPa)	f_l^* (MPa)	f_{cc}^* (MPa)	ε_{cc}^* (%)	ε_{lc}^* (%)
C50-V1F*5	51.7	1	73	13	0.18	Straight	2850	5	78.2	0.63	0.43
C50-V2F*5	64.1	2							91.1	0.64	0.45
C100-V1F*5	103.2	1							136.7	0.51	0.25
C100-V2F*5	113.5	2							157.2	0.54	0.29
C50-V1F*10	51.7	1						10	101.1	0.98	0.68
C50-V2F*10	64.1	2							127.4	0.99	0.72
C100-V1F*10	103.2	1							172.3	0.69	0.39
C100-V2F*10	113.5	2							180.1	0.73	0.44
C50-V1F*15	51.7	1						15	123.7	1.39	0.79
C50-V2F*15	64.1	2							156.1	1.40	0.84
C100-V1F*15	103.2	1							192.2	0.88	0.45
C100-V2F*15	113.5	2							203.2	0.92	0.53
C50-V1F*25	51.7	1						25	157.2	2.25	1.00
C50-V2F*25	64.1	2							196.7	2.26	1.07
C100-V1F*25	103.2	1							225.7	1.29	0.67
C100-V2F*25	113.5	2							238.3	1.33	0.79

under compression loading. The axial strain of the specimens was measured by two linear variable displacement transformers (LVDTs) mounted at the corners of steel loading and supporting plates. One axial strain gauge mounted at the mid-height of the specimen was also used to validate and correct the LVDT measurements at the early stages of the loading. Two lateral strain gauges were also placed at the mid-height of the specimen to obtain the lateral strains. Table 4 presents the compression test results of actively confined SFRCs. In the table, ε_{lc}^* is the lateral strain corresponding to f_{cc}^* and ε_{cc}^*.

2.3. Specimen designation

In specimen labels in Tables 1, 2, and 4 the numbers after V, A, F, and F* represent the V_f in percentage, A_R, actual ultimate confining pressure ($f_{lu,a}$) of FRP jacket, and f_l^* of Hoek cell in MPa, respectively. For example, V1.5A67F28 represents the FRP-confined SFRC specimen with V_f of 1.5%, A_R of 67, and $f_{lu,a}$ of 28 MPa.

3. Compressive behavior of FRP-confined SFRC

Fig. 2 shows typical axial stress-axial strain and lateral strain-axial strain curves of actively confined and FRP-confined concretes. As can be seen in the figure, the peak condition of actively confined concrete is characterized by the peak stress (f_{cc}^*) and corresponding axial strain (ε_{cc}^*) and lateral strain (ε_{lc}^*). It can also be seen in Fig. 2 that the ultimate condition of the FRP-confined concrete is characterized by the compressive strength (f'_{cc}) and corresponding axial strain (ε_{cu}) and lateral strain ($\varepsilon_{h,rup}$) recorded at the rupture of the FRP jacket.

As discussed in detail in Xie and Ozbakkaloglu [19], V_f and A_R have a notable influence on the compressive behavior of FRP-confined SFRC. It was shown in Xie and Ozbakkaloglu [19] that, at a given A_R, an increase in V_f resulted in an increase in f'_{cc}, ε_{cu}, and $\varepsilon_{h,rup}$ of FRP-confined SFRC, and an increase in A_R at a given V_f led to a decrease in these properties. These observations suggest that existing models of FRP-confined plain concrete would not be able to accurately capture the compressive behavior of FRP-confined SFRC. In this study, new expressions were developed for the hoop rupture strain, dilation relationship, and relationship between the confining pressure and the compressive strength by considering the influences of V_f and A_R on the Lim and Ozbakkaloglu's [39] expressions, which was shown to provide the most accurate predictions for FRP-confined plain concrete. It should be noted that, based on the initial assessment of experimental test results, the results of specimens containing crimped steel fibers were inconsistent with those of hooked end and straight steel fibers. Therefore, only the experimental database of hooked end and straight steel fibers were considered in the modeling. In addition, the experimental results of study by Wang et al. [37] were excluded from the modeling as these results exhibited significant fluctuations and in most cases were in disagreement with the overall trend of the database.

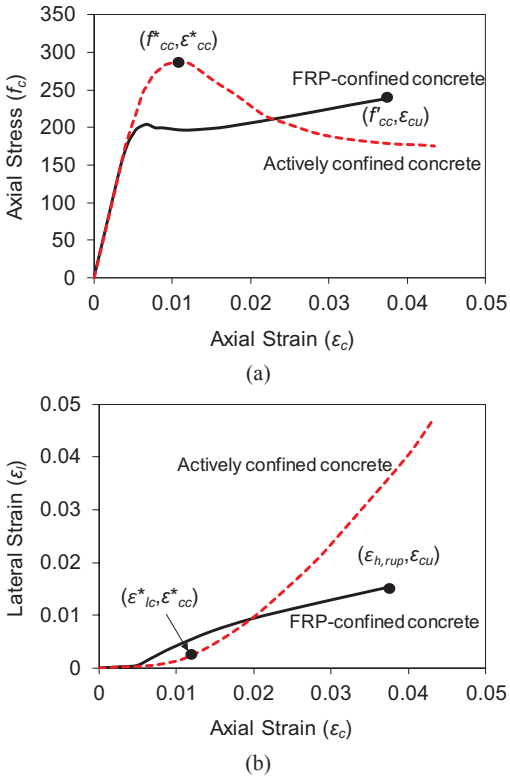

Fig. 2. (a) Typical axial stress-axial strain curves and (b) lateral strain-axial strain curves of FRP-confined and actively confined concrete (adopted from Ref. [32]).

3.1. Hoop rupture strain of FRP jacket of FRP-confined SFRC

The expression proposed by Ozbakkaloglu and Lim [11] for $\varepsilon_{h,rup}$ of FRP jacket was modified by the incorporation of the hoop rupture strain coefficient (K_1) to allow for the important influences of V_f and A_R observed in FRP-confined SFRCs.

$$\varepsilon_{h,rup} = k_{\varepsilon,rup}\varepsilon_f = K_1(0.9-2.3f'_{co} \times 10^{-3}-0.75E_f \times 10^{-6})\varepsilon_f \quad (1)$$

where $k_{\varepsilon,rup}$ and ε_f are FRP hoop strain reduction factor and ultimate tensile strain of fibers in the FRP jacket, respectively. Fig. 3(a) and (b) show the variation of experimentally determined K_1 with V_f at different

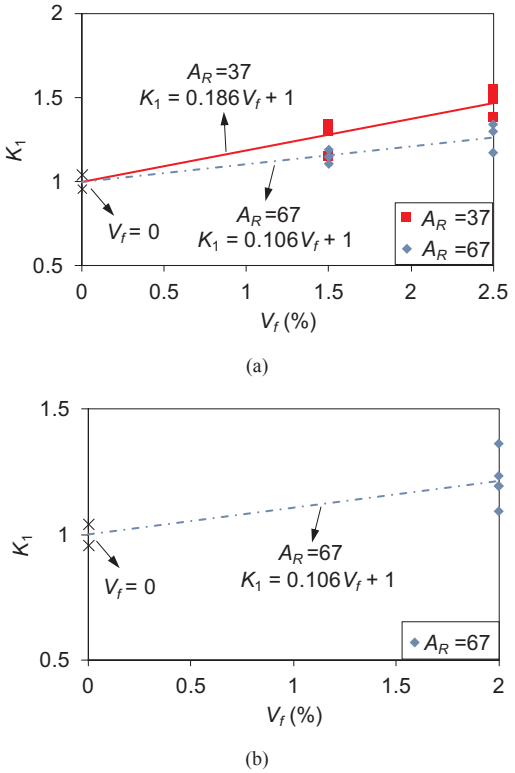

Fig. 3. Variation of experimental values of K_1 with volume fraction (V_f): concrete containing (a) hooked end; (b) straight steel fibers.

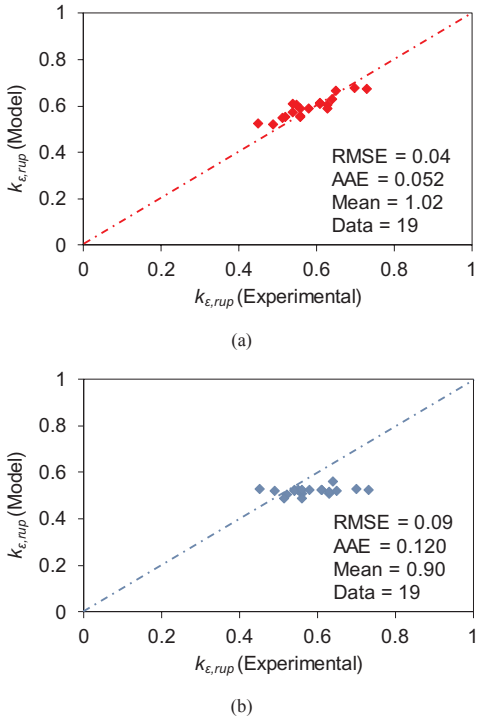

Fig. 4. Comparison of the experimental results of FRP hoop strain reduction factor ($k_{\varepsilon,rup}$) with: (a) predictions of the proposed model; (b) predictions of model by Ozbakkaloglu and Lim [11].

A_R for FRP-confined concrete containing hooked end and straight steel fibers, respectively. The experimental values of K_1 were obtained by dividing the experimental $k_{\varepsilon,rup}$ of SFRCs with the experimental $k_{\varepsilon,rup}$ of the companion plain concrete. It can be seen in Fig. 3 that the trend of the experimental K_1 of specimens containing hooked end steel fibers is consistent with that of straight steel fibers, and at a given A_R, K_1 gradually increases with an increase in V_f. This observation can be attributed to the fact that, in SFRC with higher V_f, bridges formed by steel fibers across the cracks inside the concrete lead to a more even and controlled cracking of concrete, which in turn results in the reduction of isolated major cracks in concrete and associated stress concentrations on the FRP jacket [19]. Therefore, specimens with higher V_f exhibited higher FRP hoop rupture strains. On the other hand, as can be seen in Fig. 3(a), K1 decreases with an increase in A_R at a given V_f. This can be attributed to the ability of steel fibers with lower aspect ratios to more effectively control the initiation and propagation of major cracks in concrete than their counterparts with a higher aspect ratio [37]. Based on these observations K_1 is defined as in Eq. (2) through the regression analysis of the test results.

$$K_1 = 1 + 6.1V_f/A_R \tag{2}$$

in which V_f is in percentage (%).

Fig. 4(a) and (b) show comparisons of the experimental values of $k_{\varepsilon,rup}$ with the predictions obtained by the proposed expression for $k_{\varepsilon,rup}$ (Eq. (1)) and $k_{\varepsilon,rup}$ determined by Ozbakkaloglu and Lim [11] expression, respectively. As can be seen in the figures, incorporation of K_1 into $k_{\varepsilon,rup}$ expression led to a higher accuracy over the existing model by Ozbakkaloglu and Lim [11].

3.2. Dilation behavior of confined SFRC

Analysis of the test databases of FRP-confined and actively confined SFRC revealed that the steel fiber parameters of V_f and A_R had an influence on the dilation behavior of SFRCs. It was found that the lateral strains corresponding to ε_{cu} in FRP-confined SFRC and ε^*_{cc} in actively confined SFRC increased with an increase in V_f and a decrease in A_R. The dilation relationship between lateral strain (ε_l) and axial strain (ε_c) proposed by Lim and Ozbakkaloglu [39], which was shown to be highly accurate for both actively and FRP-confined plain concrete, was modified by incorporating the dilation coefficient (K_2) into the expression to consider the key influences of steel fiber parameters.

$$\varepsilon_c = \frac{\varepsilon_l}{\upsilon\left(1+\left(\frac{\varepsilon_l}{\upsilon\varepsilon_{co}}\right)^n\right)^{\frac{1}{n}}} + 0.04\varepsilon_l^{0.7}K_2\left(1+21\left(\frac{f_l}{f'_{co}}\right)^{0.8}\right) \tag{3}$$

where υ, ε_{co}, n, and f_l are the initial Poisson's ratio of concrete, axial strain corresponding to f'_{co}, curve shape parameter, and confining pressure, respectively. In Eq. (3), f_l is a variable parameter for the FRP-confined SFRC that gradually increases with an increase in ε_l until $\varepsilon_{h,rup}$ (determined using Eq. (1)) is reached and the resulting $f_{lu,a}$ is developed. υ, ε_{co}, and n were adopted from Lim and Ozbakkaloglu [39], which are expressed as:

$$\upsilon = 8\times10^{-6}f'^{\,2}_{co} + 0.0002f'_{co} + 0.138 \tag{4}$$

$$\varepsilon_{co} = \frac{f'^{\,0.225}_{co}}{1000}\left(\frac{152}{D}\right)^{0.1}\left(\frac{2D}{H}\right)^{0.13} \tag{5}$$

$$n = 1 + 0.03f'_{co} \tag{6}$$

in which f'_{co} is in MPa and D and H are in mm. Fig. 5(a) and (b) show the variation of experimental K_2 with V_f at different A_R for FRP-confined concrete containing hooked end and straight steel fibers, respectively. As can be seen in Fig. 5, the trend of experimental K_2 of specimens containing hooked end steel fibers is consistent with that of straight steel fibers, and at a given A_R, K_2 gradually increases with an increase in V_f. This observation can be attributed to the lateral expansion of SFRC with higher V_f at a reduced rate due to the bridging effect of steel fibers [19,37]. It can also be seen in the figure that K_2 decreases with an increase in A_R at a given V_f, which can be explained by the

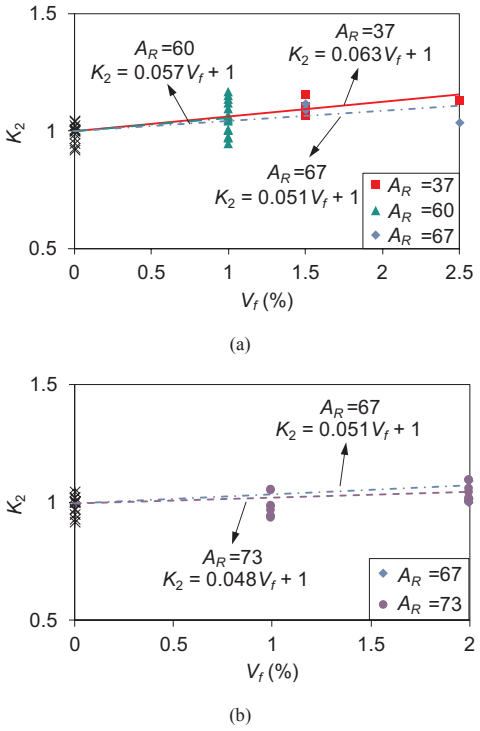

Fig. 5. Variation of experimental values of K_2 with volume fraction (V_f): concrete containing (a) hooked end; (b) straight steel fibers.

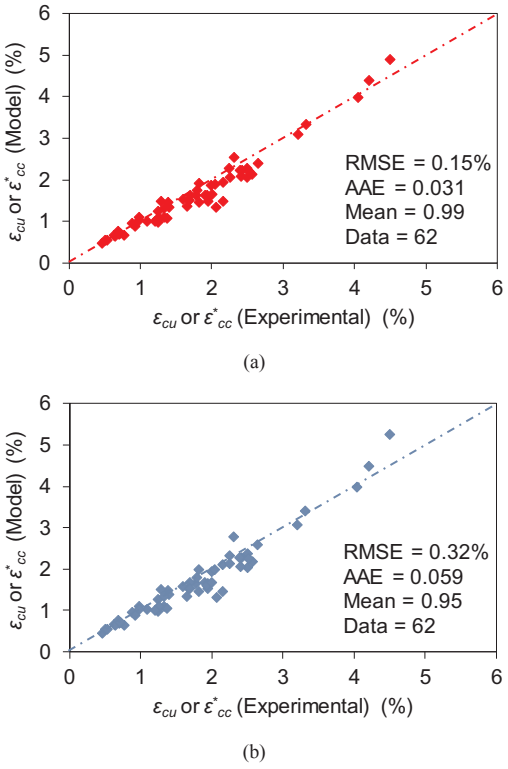

Fig. 6. Comparison of the experimental values of ultimate axial strain (ε_{cu}) or peak axial strain (ε^*_{cc}) with: (a) predictions of the proposed model; (b) predictions of model by Lim and Ozbakkaloglu [39]

lower internal confinement efficiency of steel fibers with higher A_R, leading to an increased lateral dilation rate of the resulting SFRC [19]. Based on the regression analysis, the following expression is proposed for K_2:

$$K_2 = 1 + 0.23 V_f A_R^{-0.5} \tag{7}$$

where V_f is in percentage (%).

Fig. 6 shows comparisons of the experimental values of ε_{cu} for FRP-confined SFRC and ε^*_{cc} for actively confined SFRC with the predictions obtained by the proposed expression for the dilation behavior of confined SFRC (Eq. (3)). In the calculation of ε_{cu} and ε^*_{cc} the corresponding lateral strains $\varepsilon_{h,rup}$ and ε^*_{lc} were used in Eq. (3), which were obtained from lateral strain gauges placed at the mid-height of the specimens. The experimental values of ε_{cu} and ε^*_{cc} shown in Fig. 6 were obtained from LVDTs. As can be seen in Fig. 6, incorporation of K_2 into the dilation relationship resulted in a higher prediction accuracy of the dilation behavior of FRP-confined SFRC compared to that of the model by Lim and Ozbakkaloglu [39].

3.3. Axial stress-strain relationship of FRP-confined SFRC

Through the unifying confining pressure gradient concept introduced by Lim and Ozbakkaloglu [39], the axial stress (f_c) of FRP-confined concrete can be obtained from the axial stress–strain relationship of actively confined concrete by considering the proposed confining pressure gradient ($\Delta f_l = f_l - f^*_l$, in which f_l and f^*_l are the confining pressure by FRP confinement and corresponding confining pressure by active confinement, respectively). In this study, actively confined concrete model proposed by Lim and Ozbakkaloglu [42], which was modified from Popovics model [43], was used to obtain the axial stress-strain curves of actively confined concretes. Defining the axial stress-strain curve of actively confined concrete requires the accurate determination of the coordinates of the curve corresponding to the peak stress (i.e. f^*_{cc} and ε^*_{cc}). Based on the analysis of the test database it is found that steel fiber properties, such as V_f and A_R, did not have a significant influence on ε^*_{cc} of actively confined SFRCs. Therefore, in the current study a new expression was developed only for f^*_{cc} of SFRCs and it is recommended that the ε^*_{cc} expression given by Lim and Ozbakkaloglu [42] (i.e. $\varepsilon^*_{cc} = \varepsilon_{co} + 0.045(f^*_l/f'_{co})^{1.15}$) for actively confined plain concrete can also be applied to actively confined SFRC. f^*_{cc} expression proposed by Lim and Ozbakkaloglu [42] for plain concrete was modified by incorporating the strength coefficient (K_3) into the expression.

$$f^*_{cc} = f'_{co} + 5.2 K_3 f'^{\,0.91}_{co} \left(\frac{f^*_l}{f'_{co}}\right)^a \quad \text{where a} = f'^{\,-0.06}_{co} \tag{8}$$

Fig. 7(a) and (b) show the variation of experimental K_3 with V_f for FRP-confined concrete containing hooked end and straight steel fibers, respectively. As can be seen in the figures, K_3 gradually increases with an increase in V_f, which is attributed to the additional confinement provided by the internal steel fibers resulting in enhancements in the compressive strength of SFRCs [37]. The regression analysis showed that V_f was the only influential parameter for f^*_{cc}. However, it is worth noting that this observation is limited to mixes prepared with a relatively narrow range of A_R spanning from 60 to 73 due to the limitations of the current database. Accordingly, K_3 is defined through Eq. (9) as a function of V_f.

$$K_3 = 1 + 0.065 V_f \tag{9}$$

in which V_f is in percentage (%).

Fig. 8(a) and (b) show comparisons of the experimental values of f^*_{cc} with the predictions obtained by the proposed expression for f^*_{cc} (Eq. (5)) and f^*_{cc} determined by Lim and Ozbakkaloglu [42] expression, respectively. As can be seen in the figures, incorporation of K_3 into f^*_{cc} expression led to a higher a prediction accuracy compared with that of the model by Lim and Ozbakkaloglu [42].

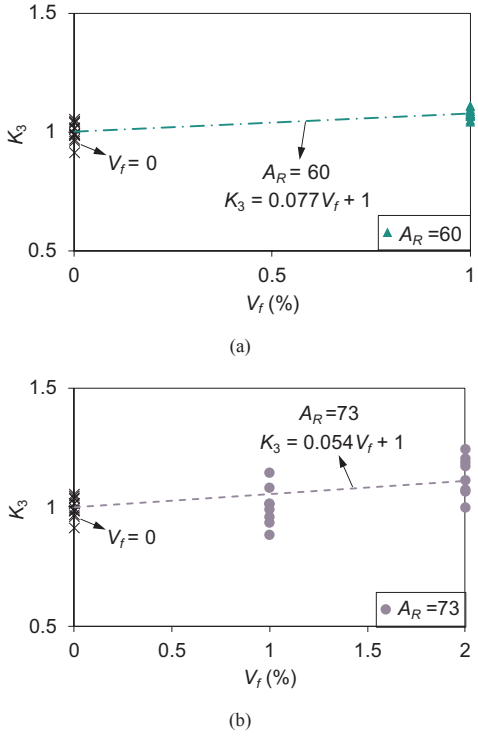

Fig. 7. Variation of experimental values of K_3 with volume fraction (V_f): concrete containing (a) hooked end; (b) straight steel fibers.

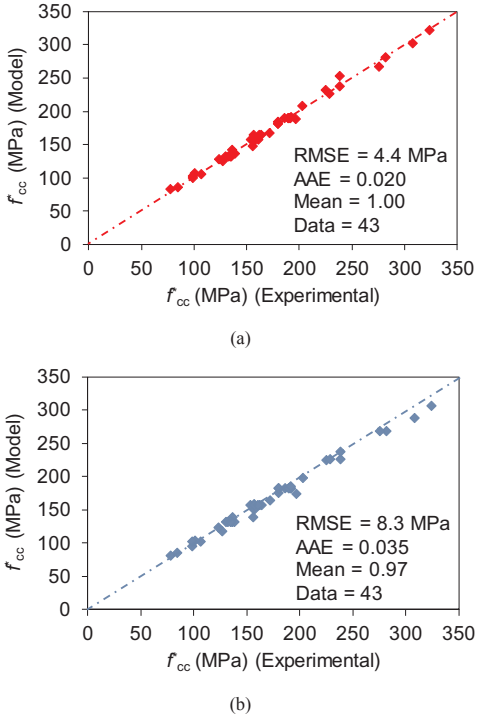

Fig. 8. Comparison of the experimental values of peak axial stress (f'_{cc}) with: (a) predictions of the proposed model; (b) predictions of model by Lim and Ozbakkaloglu [42]

4. FE modeling of compressive behavior of FRP-confined SFRC

As was discussed in Refs. [31,34], different theories of plasticity, damage, and coupled damage-plasticity have been proposed for FE modeling of concrete [26,35,36,44–47]. Plasticity approach only considers a plasticity failure surface and does not address the degradation of the material stiffness [26]. Conversely, the damage approach only applies the degradation of the material stiffness without considering the irreversible deformations and inelastic volumetric expansion in compression [44]. On the other hand, the concrete damage-plasticity approach combines the benefits of both plasticity and damage approaches in the failure surface and flow rule. Therefore, the concrete damage-plasticity method, which was developed by Ozbakkaloglu et al. [31] and Lim et al. [34], was adopted in the present study for FE modeling of FRP-confined SFRCs.

Appendix B presents the details of the concrete damage-plasticity method given in Refs. [31,34]. The new expressions proposed in the current study for f'_{cc} (Eq. (8)), $\varepsilon_{h,rup}$ (Eq. (1)), and the axial strain-lateral strain relationship (Eq. (3)) were adopted to improve the failure surface and flow rule of the concrete damage-plasticity model for FRP-confined SFRC. The improved failure surface and flow rule were achieved through the use of Eq. (8) in Eq. (17) (in Appendix B) and Eq. (3) in Eq. (20) (in Appendix B), respectively. The proposed model is applicable to confined SFRCs containing hooked end and straight steel fibers with up to 194 MPa unconfined concrete strength.

5. Comparison of proposed model predictions with experimental results

The FRP-confined SFRC specimens were modeled in FE program ABAQUS using the proposed constitutive model. As was done previously in Refs. [31,34], boundary conditions were assigned to the axis-symmetric planes and were considered to be pinned-end to simulate the specimen boundary conditions in the test setup. A tie constraint was used to model the interaction between the FRP sheet and concrete, through which the nodes on both surfaces were constrained to displace similarly. FRP sheets were modeled by four-node shell elements with reduced integration (S4R) and the concrete core was modeled as the eight-node brick element (C3D8R). To capture the post-peak softening behavior of concrete, axial compression was applied as a uniform axial displacement to the nodes along the top of the specimen. Compressive stresses and strains were defined to be positive. Fig. 9 shows a typical FRP-confined SFRC specimen modeled in ABAQUS. In order to validate the proposed model, the predictions obtained from the FE analysis based on the model were compared with the experimental results of FRP-confined SFRC and predictions of the model by Lim and Ozbakkaloglu [39] proposed for FRP-confined plain concrete. Four groups of FRP-confined SFRC specimens (i.e. U120-1, U120-2, U190-1, and U190-2) were used in the validation of the FE model. Figs. 10 and 11 show the axial stress-axial strain, lateral strain-axial strain, axial stress-volumetric strain, plastic volumetric strain-axial plastic strain, and plastic dilation angle-axial plastic strain relationships for the group U120-1 and U120-2 specimens (refer to Table 1 for specimen properties),

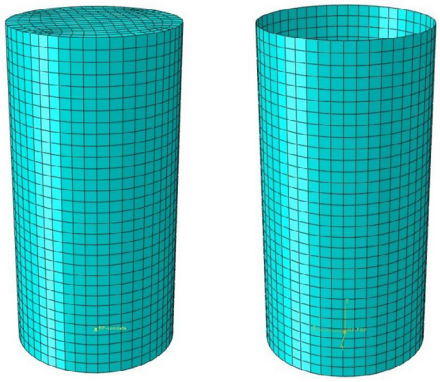

Fig. 9. FE modeling of FRP-confined SFRC: (a) SFRC; (b) FRP tube.

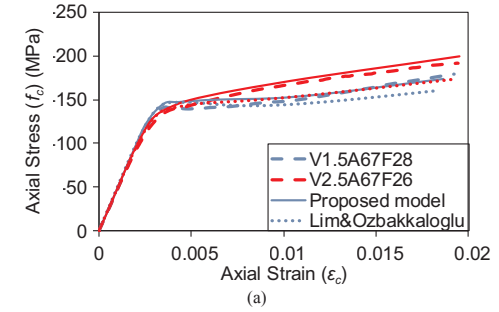

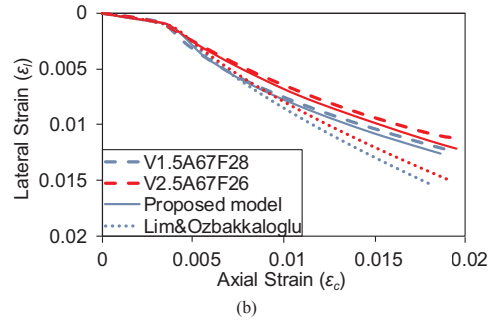

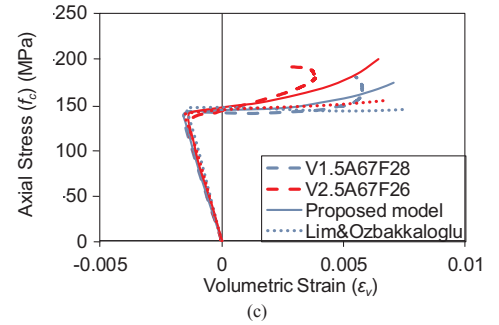

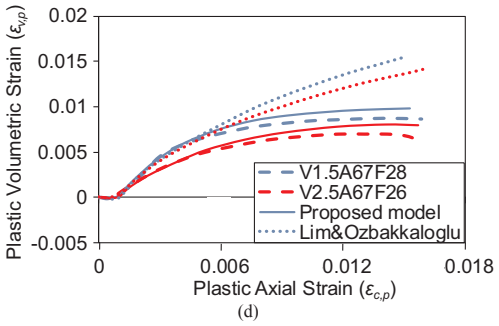

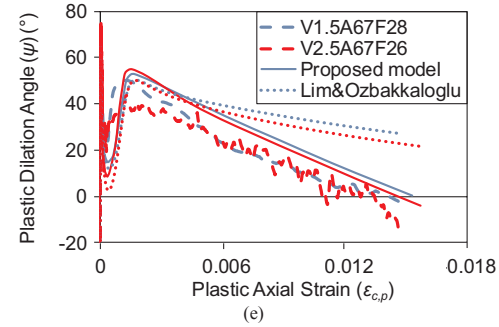

Fig. 10. Variation of: (a) axial stress-axial strain; (b) lateral strain-axial strain; (c) axial stress-volumetric strain; (d) plastic volumetric strain-axial plastic strain; (e) plastic dilation angle-axial plastic strain relationships of Group U120-1.

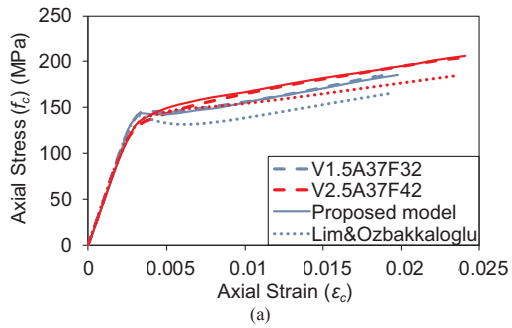

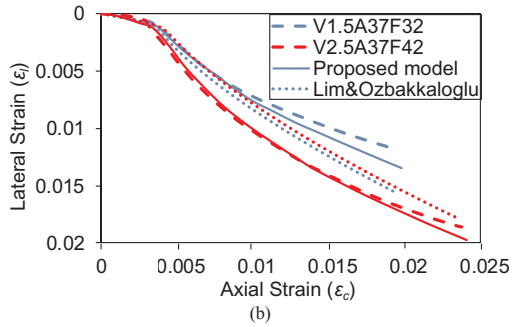

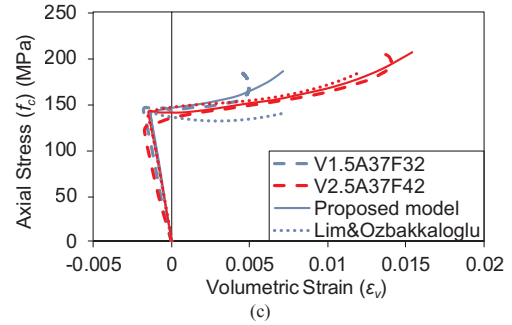

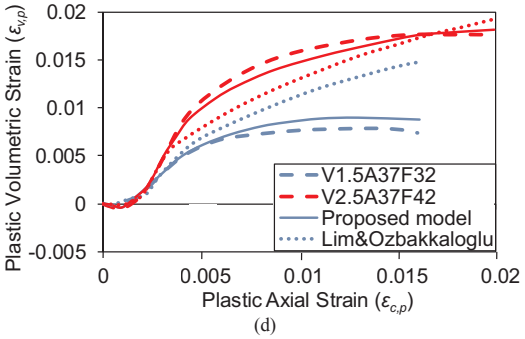

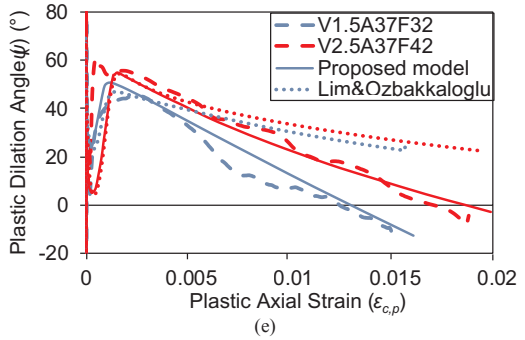

Fig. 11. Variation of: (a) axial stress-axial strain; (b) lateral strain-axial strain; (c) axial stress-volumetric strain; (d) plastic volumetric strain-axial plastic strain; and (e) plastic dilation angle-axial plastic strain relationships of Group U120-2.

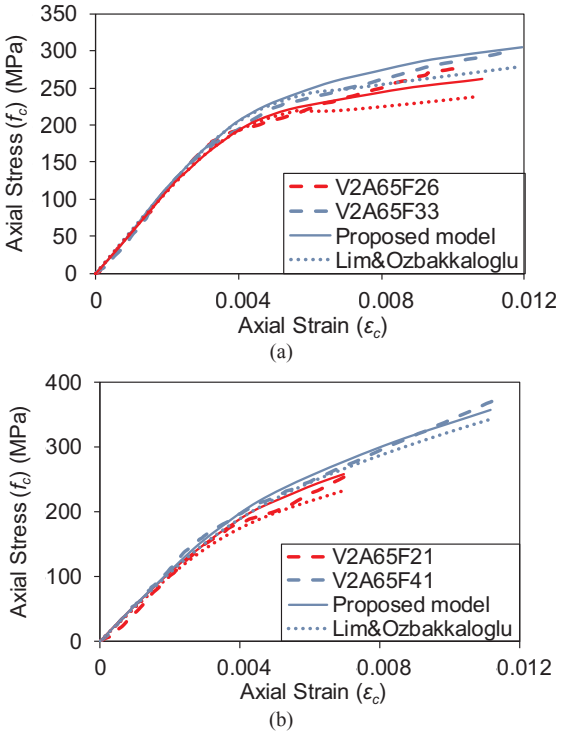

Fig. 12. Variation of axial stress-axial strain relationships for Groups: (a) U190-1; (b) U190-2.

whereas Fig. 12 shows the axial stress-axial strain relationships for the group U190-1 and U190-2 specimens.

As can be seen in Figs. 10–12, the proposed model closely predicts the mechanical behavior of FRP-confined SFRCs and it provides higher accuracy than the predictions of the model by Lim and Ozbakkaloglu, which shows considerable deviations from the experimental test results of FRP-confined SFRCs. The accuracy of the proposed model was achieved by the incorporation of the key internal steel fiber properties (i.e. V_f and A_R) into the accurate failure surface and flow rule models given for plain concrete in Refs. [31,34]. As can be seen in Figs. 10(a) and 11(a), model by Lim and Ozbakkaloglu significantly underestimated the stresses in the axial stress-axial strain relationship of FRP-confined SFRCs, especially for specimens with a higher steel fiber volume fraction. Figs. 10(b) and 11(b) show the lateral strain-axial strain relationships of FRP-confined SFRC specimens of the group U120-1 and U120-2, respectively. The higher accuracy of the proposed FE model compared to the model by Lim and Ozbakkaloglu in prediction of the dilation behavior of FRP-confined SFRC is because of the incorporation of the steel fiber parameters (V_f and A_R) in the prediction of the hoop rupture strain and relationship between axial and lateral strains.

Figs. 10(c) and 11(c) show the axial stress-volumetric strain relationships of FRP-confined SFRC under different steel fiber parameters and levels of confinement. As can be seen in the figures, inelastic volumetric contraction occurred at the beginning of the plastic flow and followed by dilation. It means that the volume of each SFRC specimen contracted until the specimen reached its unconfined concrete strength. After this point, the lateral restraint resulted in a change from contraction to expansion throughout the loading history. As can be seen in Figs. 10(d) and 11(d), which show the plastic volumetric strain-plastic axial strain relationships for FRP-confined SFRC, the sign of the tangential slope of the curve changed from negative to positive at an inflection point (transition point from the first to second part of the curve), which verifies the transition from contraction to expansion seen in Figs. 10(c) and 11(c). It can be seen in Figs. 10(e) and 11(e), which show the plastic dilation angle-plastic axial strain relationships for FRP-confined SFRC, that plastic dilation angle (ψ) decreases with an increase in the plastic axial strain until the inflection point of Figs. 10(d) and 11(d) and then it rapidly increases until the plastic volumetric strain becomes zero, which corresponds to the transition from contraction to expansion seen in Figs. 10(c) and 11(c). With an increase in the level of confining pressure under FRP confinement, the concrete dilatancy has a tendency to change towards densification, which can be seen as the reduction in ψ with a further increase in the plastic axial strain in Figs. 10(e) and 11(e).

Fig. 12 shows the axial stress-axial strain curves of FRP-confined ultra high-strength SFRC, from which it can be seen that the curves obtained by the proposed model are in close agreement with the experimental curves. These results indicate that the proposed FE model can be applied to predict the compressive behavior of circular FRP-confined SFRC specimens with an unconfined concrete strength of up to 194 MPa.

6. Summary and conclusions

This paper has presented the first FE model to predict the compressive behavior of FRP-confined SFRCs in circular sections. A test database containing 73 datasets from axial compression tests of FRP-confined and actively confined SFRC was assembled based on the results available in the literature. Additional axial compression tests were conducted on 16 actively confined SFRC specimens to address the gaps in the existing test database. The analysis of the experimental test results indicated that the compressive behavior of FRP-confined SFRC is influenced by the steel fiber volume fraction and aspect ratio. Therefore, the model by Lim and Ozbakkaloglu, which was proposed for FRP-confined plain concretes, was extended to predict the compressive behavior of FRP-confined SFRCs by considering the influences of steel fiber volume fraction and aspect ratio. In the proposed model, the hoop rupture strain of the FRP jacket, dilation relationship between axial strain and lateral strain of actively confined and FRP-confined SFRC, and relationship between the confining pressure and the compressive strength of actively confined SFRC were established by modifying the previously proposed models for confined plain concrete. The improved failure surface and flow rule of the concrete damage-plasticity model were achieved by incorporating the effects of steel fiber volume fraction and aspect ratio into the accurate failure surface and flow rule models given for plain concrete in Refs. [31,34]. The comparison of model predictions with the experimental results shows that the new models closely predict the axial stress-axial strain, lateral strain-axial strain, axial stress-volumetric strain, plastic volumetric strain-axial plastic strain, and plastic dilation angle-axial plastic strain relationships of FRP-confined SFRC. The analysis results also indicate that the new FE model provides improved accuracy in predicting the compressive behavior of FRP-confined SFRCs compared to the predictions of the model given by Lim and Ozbakkaloglu for conventional concrete. The availability of such an accurate model is of vital importance for practical applications of FRP-confined SFRC columns.

Because of the influence of the steel fiber parameters on the mechanical behavior of FRP-confined SFRC, the application of the models of FRP-confined plain concrete to predict the behavior of FRP-confined SFRC is not recommended. Therefore, additional targeted studies are recommended on the FRP-confined and actively confined SFRC columns to expand the existing test database to enable the development of additional models for FRP-confined SFRCs with a broader range of applicability, such as those for square and rectangular columns.

Acknowledgements

The authors gratefully acknowledge the support from the National Natural Science Foundation of China through Grant No. 51650110495 and the University of Adelaide through a Research Excellence Grant awarded to the second author. The authors also thank Mr. Liu and

Mesdames Yang and Liu for completing the tests reported in this paper as part of their Master's thesis.

Appendix A. Supplementary data

The script code used for the concrete material behavior based on the developed damage-plasticity model. Supplementary data associated with this article can be found, in the online version, at http://dx.doi.org/10.1016/j.compstruct.2018.03.094.

Appendix B. Concrete damage-plasticity model

This section presents the details of the concrete damage-plasticity method used in this study. The failure surface of the concrete damage-plasticity method is presented by Eq. (10) [36].

$$F = \frac{1}{1-\alpha}(\bar{q}-3\alpha\bar{p} + \beta(\tilde{\varepsilon}_p)\langle-\hat{\bar{\sigma}}_{min}\rangle-\gamma\langle\hat{\bar{\sigma}}_{min}\rangle)-\bar{\sigma}_c(\tilde{\varepsilon}_{c,p}) \leqslant 0 \tag{10}$$

where $\hat{\bar{\sigma}}_{min}$ is the minimum principal effective stress and the parameters $\bar{p}$, $\bar{q}$, α, $\beta\tilde{\varepsilon}_p$, and γ are defined in Eqs. 11–15, respectively.

$$\bar{p} = \frac{-\bar{I}_1}{3} \tag{11}$$

$$\bar{q} = \sqrt{3\bar{J}_2} \tag{12}$$

$$\alpha = \frac{f'_{bo}-f'_{co}}{2f'_{co}-f'_{co}} \tag{13}$$

$$\beta(\tilde{\varepsilon}_p) = \frac{\bar{\sigma}_c(\tilde{\varepsilon}_{c,p})}{\bar{\sigma}_t(\tilde{\varepsilon}_{t,p})}(1-\alpha)-(1 + \alpha) \tag{14}$$

$$\gamma = \frac{3(1-K_c)}{2K_c-1} \text{ where } K_c = \frac{q_{tm}}{q_{cm}} \tag{15}$$

where $\bar{p}$ is the equivalent effective stress, $\bar{q}$ is the cylindrical coordinates of equivalent pressure, $\bar{I}_1$ and $\bar{J}_2$ are the first invariant of effective stress and second invariant of the effective stress deviator, f'_{bo} and f'_{co} are the biaxial and uniaxial compressive strengths, $\bar{\sigma}_c$ and $\bar{\sigma}_t$ are the effective compressive and tensile cohesion stresses, $\tilde{\varepsilon}_{c,p}$ and $\tilde{\varepsilon}_{t,p}$ are the equivalent compressive and tensile plastic strains, and q_{tm} and q_{cm} are the second stress invariants on the tensile and compression meridians, respectively. As was shown in Refs. [31,34], f'_{bo}/f'_{co} and tensile-to-compression meridian stress ratio (K_c) are defined as $1.57f'^{-0.09}_{co}$ and $0.71f'^{-0.025}_{co}$, respectively, which were obtained based on a large experimental database of confined plain concrete.

Parameter of α in Eq. (14) is defined by the following expression for addressing the exact and curve shape compression and tensile meridians while satisfying the original form of f'_{bo}/f'_{co} ratio.

$$\alpha = \frac{k_b-1}{2 + k_b}\left(\frac{\gamma}{3} + 1\right)-\frac{\gamma}{3} \tag{16}$$

in which k_b is the enhancement ratio of f^*_{cc} under uniform confining pressure (f^*_l) and it is obtained from the following expression:

$$k_b = \frac{f^*_{cc}-f'_{co}}{f^*_l} \tag{17}$$

Eq. (8) is used to establish a relationship between f^*_{cc} and f^*_l in Eq. (17).

The non-associated potential flow rule with the plastic potential function (G) and the plastic strain vector ($d\varepsilon_p$) are defined by Eqs. (18) and (19) in concrete damage-plasticity theory, respectively.

$$G = \sqrt{(\varepsilon f'_t\tan\psi)^2 + \bar{q}^2}-\bar{p}\tan\psi \tag{18}$$

$$d\varepsilon_p = \lambda\frac{\partial G}{\partial\sigma} \tag{19}$$

in which ψ is the plastic dilation angle measured in the $\bar{p}-\bar{q}$ plane at high confining pressure, f'_t is the uniaxial tensile strength, and ε is the eccentricity parameter that defines the rate at which the G function tends to a straight line as the eccentricity tends to zero. The relationship between ψ and plastic strains is defined by Eq. (20) [29].

$$\tan\psi = -\frac{3(d\varepsilon_{c,p} + 2d\varepsilon_{l,p})}{2(d\varepsilon_{c,p}-d\varepsilon_{l,p})} \tag{20}$$

For calculating ψ, Eq. (3) is used to define the relationship between the axial strain (ε_c) and lateral strain (ε_l) of FRP-confined SFRCs. In Eq. (3), f_l is a variable parameter for the FRP-confined SFRC that gradually increases with an increase in ε_l until $\varepsilon_{h,rup}$ (determined using Eq. (1)) is reached and the resulting $f_{lu,a}$ is developed.

References

[1] Lu X, Hsu CT. Behavior of high strength concrete with and without steel fiber reinforcement in triaxial compression. Cem Concr Res 2006;36:1679–85.
[2] Bencardino F, Rizzuti L, Spadea G, Swamy RN. Stress-strain behavior of steel fiber-reinforced concrete in compression. J Mater Civil Eng 2008;20(3):255–63.
[3] Kaïkea A, Achoura D, Duplan F, Rizzuti L. Effect of mineral admixtures and steel fiber volume contents on the behavior of high performance fiber reinforced concrete. Mater Des 2014;63:493–9.
[4] Madandoust R, Ranjbar MM, Ghavidel R, Shahabi F. Assessment of factors influencing mechanical properties of steel fiber reinforced self-compacting concrete. Mater Des 2015;83:284–94.
[5] Ilki A, Peker O, Karamuk E, Demir C, Kumbasar N. FRP retrofit of low and medium strength circular and rectangular reinforced concrete columns. J Mater Civil Eng 2008;20(2):169–88.
[6] Doran B, Koksal HO, Turgay T. Nonlinear finite element modeling of rectangular/square concrete columns confined with FRP. Mater Des 2009;30(8):3066–75.
[7] Kusumawardaningsih Y, Hadi MNS. Comparative behaviour of hollow columns confined with FRP composites. Compos Struct 2010;93(1):198–205.
[8] Smith ST, Kim SJ, Zhang H. Behavior and effectiveness of FRP wrap in the confinement of large concrete cylinders. J Compos Construct 2010;14(5):573–82.
[9] Rousakis T, Karabinis A, Kiousis P, Tepfers R. Analytical modeling of plastic behavior of uniformly FRP confined concrete members. Compos Part B Eng 2008;39(7–8):1104–13.
[10] Wu YF, Jiang JF. Effective strain of FRP for confined circular concrete columns. Compos Struct 2013;95:479–91.
[11] Ozbakkaloglu T, Lim JC. Axial compressive behavior of FRP-confined concrete: experimental test database and a new design-oriented model. Compos Part B Eng 2013;55:607–34.
[12] Vincent T, Ozbakkaloglu T. Influence of concrete strength and confinement method on axial compressive behavior of FRP confined high- and ultra high-strength concrete. Compos Part B Eng 2013;50:413–28.
[13] Lim JC, Ozbakkaloglu T. Confinement model for FRP-confined high-strength concrete. J Compos Construct 2014;18(4):04013058.
[14] Ozbakkaloglu T, Vincent T. Axial compressive behavior of circular high-strength concrete-filled FRP tubes. J Compos Construct 2014;18(2):04013037.
[15] Ozbakkaloglu T. A novel FRP-dual grade concrete-steel composite column system. Thin Wall Struct 2015;96:295–306.
[16] Mansouri I, Gholampour A, Kisi O, Ozbakkaloglu T. Evaluation of peak and residual conditions of actively confined concrete using neuro-fuzzy and neural computing techniques. Neural Comput Appl 2018;29. http://dx.doi.org/10.1007/s00521-016-2492-4.
[17] Ozbakkaloglu T, Louk Fanggi BA, Zheng J. Confinement model for concrete in circular and square FRP-concrete-steel double skin-composite columns. Mater Des 2016;96:458–69.
[18] Afroughsabet V, Biolzi L, Ozbakkaloglu T. High performance fiber-reinforced concrete: a review. J Mater Sci 2016;51(14):6517–51.
[19] Xie T, Ozbakkaloglu T. Behavior of steel fiber-reinforced high-strength concrete-filled FRP tube columns under axial compression. Eng Struct 2015;90:158–71.
[20] Zohrevand P, Mirmiran A. Stress-strain model of ultrahigh performance concrete confined by fiber-reinforced polymers. J Mater Civil Eng 2013;25(12):1822–9.
[21] Dundar C, Erturkmen D, Tokgoz S. Studies on carbon fiber polymer confined slender plain and steel fiber reinforced concrete columns. Eng Struct 2015;102:31–9.
[22] Deng ZC, Qu JL. The experimental studies on behavior of ultrahigh-performance concrete confined by hybrid fiber-reinforced polymer tubes. Adv Mater Sci Eng 2015. http://dx.doi.org/10.1155/2015/201289.
[23] Mirmiran A, Zagers K, Yuan WQ. Nonlinear finite element modeling of concrete confined by fiber composites. Finite Elem Anal Des 2000;35(1):79–96.
[24] Malvar LJ, Morrill KB, Crawford JE. Numerical modeling of concrete confined by fiber-reinforced composites. J Compos Construct 2004;8(4):315–22.
[25] Karabinis AI, Rousakis TC, Manolitsi GE. 3D finite-element analysis of substandard RC columns strengthened by fiber-reinforced polymer sheets. J Compos Construct 2008;12(5):531–40.
[26] Yu T, Teng JG, Wong YL, Dong SL. Finite element modeling of confined concrete-I: Drucker-Prager type plasticity model. Eng Struct 2010;32(3):665–79.
[27] Yu T, Teng JG, Wong YL, Dong SL. Finite element modeling of confined concrete-II: plastic-damage model. Eng Struct 2010;32(3):680–91.
[28] Csuka B, Kollar LP. Analysis of FRP confined columns under eccentric loading. Compos Struct 2012;94(3):1106–16.
[29] Jiang JF, Wu YF. Identification of material parameters for Drucker-Prager plasticity model for FRP confined circular concrete columns. Int J Solids Struct 2012;49(3–4):445–56.
[30] Youssf O, ElGawady MA, Mills JE, Ma X. Finite element modelling and dilation of FRP-confined concrete columns. Eng Struct 2014;79:70–85.
[31] Ozbakkaloglu T, Gholampour A, Lim JC. Damage-plasticity model for FRP-confined normal-strength and high-strength concrete. J Compos Construct 2016. http://dx.doi.org/10.1061/(ASCE)CC.1943-5614.0000712.
[32] Lim JC, Ozbakkaloglu T. Investigation of the influence of application path of confining pressure: tests on actively confined and FRP-confined concretes. J Struct Eng 2015. http://dx.doi.org/10.1061/(ASCE)ST.1943-541X.0001177.
[33] Lim JC, Ozbakkaloglu T. Lateral strain-to-axial strain relationship of confined concrete. J Struct Eng 2015. http://dx.doi.org/10.1061/(ASCE)ST.1943-541X.0001094.
[34] Lim JC, Ozbakkaloglu T, Gholampour A, Bennett T, Sadeghi R. Finite-element modeling of actively confined normal-strength and high-strength concrete under uniaxial, biaxial, and triaxial compression. J Struct Eng 2016. http://dx.doi.org/10.1061/(ASCE)ST.1943-541X.0001589.
[35] Lubliner J, Oliver J, Oller S, Onate E. A plastic-damage model for concrete. Int J Solids Struct 1989;25(3):299–326.
[36] Lee J, Fenves GL. Plastic-damage model for cyclic loading of concrete structures. J Eng Mech 1998;124(8):892–900.
[37] Wang ZL, Zhu HH, Wang JG, Zhu B. Experimental study on macroscopic mechanical behavior of SFRC under triaxial compression. Mech Adv Mater Struct 2012;19(8):653–62.
[38] ABAQUS. ABAQUS Analysis User's Manual, version 6.12. Providence, RI, USA: Dassault Systèmes Simulia Corp.; 2012.
[39] Lim JC, Ozbakkaloglu T. Unified stress-strain model for FRP and actively confined normal-strengh and high-strength concrete. J Compos Construct 2015;19(4):04014072.
[40] ASTM C143/C143M-12. Standard test method for slump of hydraulic-cement concrete. West Conshohocken: ASTM International; 2012.
[41] ASTM C39/C39M-16b. Standard test method for compressive strength of cylindrical concrete specimens. West Conshohocken, PA, USA: ASTM International; 2016.
[42] Lim JC, Ozbakkaloglu T. Stress-strain model for normal- and light-weight concretes under uniaxial and triaxial compression. Construct Build Mater 2014;71:492–509.
[43] Popovics S. A numerical approach to the complete stress-strain curves for concrete. Cem Concr Res 1973;3(5):583–99.
[44] Lubarda VA, Kracjinvovic D, Mastilovic S. Damage model for brittle elastic solids with unequal tensile and compressive strength. Eng Fract Mech 1994;49:681–97.
[45] Imran I, Pantazopoulou SJ. Plasticity model for concrete under triaxial compression. J Eng Mech 2001;127(3):281–90.
[46] Karabinis AI, Rousakis TC. Concrete confined by FRP material: a plasticity approach. Eng Struct 2002;24(7):923–32.
[47] Zheng F, Wu Z, Gu C, Bao T, Hu J. A plastic damage model for concrete structure cracks with two damage variables. Sci China Tech Sci 2012;55(11):2971–80.